



Smearred Multiscale Finite Element Models for Mass Transport and Electrophysiology Coupled to Muscle Mechanics

Milos Kojic^{1,2,3*}, Miljan Milosevic^{2,4}, Vladimir Simic², Bogdan Milicevic², Vladimir Geroski², Sara Nizzero^{1,5}, Arturas Ziemys¹, Nenad Filipovic⁶ and Mauro Ferrari¹

¹ Department of Nanomedicine, Houston Methodist Research Institute, Houston, TX, United States, ² Bioengineering Research and Development Center BioIRC Kragujevac, Kragujevac, Serbia, ³ Serbian Academy of Sciences and Arts, Belgrade, Serbia, ⁴ Faculty of Information Technologies, Belgrade Metropolitan University, Belgrade, Serbia, ⁵ Applied Physics Graduate Program, Rice University, Houston, TX, United States, ⁶ Faculty for Engineering Sciences, University of Kragujevac, Kragujevac, Serbia

OPEN ACCESS

Edited by:

Stefan Scheiner,
Vienna University of
Technology, Austria

Reviewed by:

Tamer Abdalrahman,
Charité Medical University of
Berlin, Germany
Stephane Avril,
Ecole des Mines de
Saint-Étienne, France

*Correspondence:

Milos Kojic
mkojic42@gmail.com

Specialty section:

This article was submitted to
Biomechanics,
a section of the journal
Frontiers in Bioengineering and
Biotechnology

Received: 19 July 2019

Accepted: 15 November 2019

Published: 10 December 2019

Citation:

Kojic M, Milosevic M, Simic V,
Milicevic B, Geroski V, Nizzero S,
Ziemys A, Filipovic N and Ferrari M
(2019) Smearred Multiscale Finite
Element Models for Mass Transport
and Electrophysiology Coupled to
Muscle Mechanics.
Front. Bioeng. Biotechnol. 7:381.
doi: 10.3389/fbioe.2019.00381

Mass transport represents the most fundamental process in living organisms. It includes delivery of nutrients, oxygen, drugs, and other substances from the vascular system to tissue and transport of waste and other products from cells back to vascular and lymphatic network and organs. Furthermore, movement is achieved by mechanical forces generated by muscles in coordination with the nervous system. The signals coming from the brain, which have the character of electrical waves, produce activation within muscle cells. Therefore, from a physics perspective, there exist a number of physical fields within the body, such as velocities of transport, pressures, concentrations of substances, and electrical potential, which is directly coupled to biochemical processes of transforming the chemical into mechanical energy and further internal forces for motion. The overall problems of mass transport and electrophysiology coupled to mechanics can be investigated theoretically by developing appropriate computational models. Due to the enormous complexity of the biological system, it would be almost impossible to establish a detailed computational model for the physical fields related to mass transport, electrophysiology, and coupled fields. To make computational models feasible for applications, we here summarize a concept of smearred physical fields, with coupling among them, and muscle mechanics, which includes dependence on the electrical potential. Accuracy of the smearred computational models, also with coupling to muscle mechanics, is illustrated with simple example, while their applicability is demonstrated on a liver model with tumors present. The last example shows that the introduced methodology is applicable to large biological systems.

Keywords: mass transport, drug delivery, electrophysiology, muscle mechanics, tumor model, liver, composite smearred finite element

INTRODUCTION

Convection and diffusion are the fundamental processes regarding transport of molecules or particles (e.g., nanoparticles used in drug delivery) from the cardiovascular system to tissue and interior (cytosol and organelles) (Rushmer, 1976; Hall, 2016). The route of this mass transport goes from blood or lymph to (microenvironment), from extracellular space to intracellular space,

and finally to organelles. Along that bidirectional path, molecules/particles pass through the well-known biological barriers: vessel walls and cell and organelle membranes.

The interdisciplinary scientific field where the mass transport is studied, related to drug delivery by applying nanoparticles as the drug carriers to tumor sites, is named oncophysics (Ferrari, 2010; Koay and Ferrari, 2014; Blanco et al., 2015). The fundamental physical principles that govern the mass transport rely on the pressure gradient in case of convection and on concentration gradient in case of diffusion. Of course, the physical process is affected by the physical and chemical characteristics of the transported molecules or particles and the surrounding medium (Reulen et al., 1977; Popel and Pittman, 1998).

Blood as the basic fluid carrying nutrients, oxygen, drugs, and so on is a complex medium, and in computational models, certain approximations have to be adopted. In large vessels, this approximation is made by modeling blood as a homogenous fluid with certain viscosity properties (Shi et al., 2011), where the molecular transport is governed by convective-diffusive laws. This approximation is less valid in small vessels, such as capillaries (diameter size on the order of $10\ \mu\text{m}$; Mathura et al., 2001) where the presence of cells, mainly red blood cells (RBCs), affects transport (D'Apolito et al., 2015); still, in a simplified analysis, blood may be considered as a homogenous fluid with appropriate viscosity (Sevick and Jain, 1989b; Cinar et al., 1999). Complexity of the capillary network can be seen in various references (e.g., Skinner et al., 1990; Ma and Zhang, 1998), and images are available today on the Internet.

Tissue is a complex medium through which the mass transport occurs, but, regarding the computational modeling, it has to be approximated; the degree of approximation goes from an isotropic continuum to detailed description of extracellular space, cells, and cell interior. Extensive experimental research has been carried out over decades; we cite few recent, as molecule transport within brain tissue (Nicholson, 2001) or (Swabb et al., 1974) where tissue glycosaminoglycan content and drug molecular weight were found to be important parameters determining whether extravascular transport is governed by diffusion or convection. Khaled and Vafai (2003) presented a review of models used for convection and diffusion, including heat transfer, whereas Nugent and Jain (1984) and Gerlowski and Jain (1986) studied diffusivity of dextran molecules in tumor interstitium.

Transport through biological barriers as vessel walls, or cell and organelle membranes, depends on the transport properties of these barriers, as hydraulic or diffusion coefficients, and on the size of the surface that separates the continuum domains. As an illustration, we cite here measurements of the volumes and cross-sectional areas of blood vessels of a dog (Rushmer, 1976), which show that the mass exchange occurs mostly at the capillary-tissue level. The capillary volumetric fraction (capillary density) is one of the important characteristics in the mass exchange (Kojic et al., 2017b), which will represent a basic parameter in our computational models.

As will be seen in the formulation of our computational models, we will rely on the usually adopted governing laws for

transport within extracellular space: the Darcy velocity–pressure relationship for convection and Fick's law for diffusion (Kojic et al., 2008). Transport within tumors has additional complexities due to variability of vessel diameters and lengths (Roberts and Palade, 1997) and irregular blood vessel branching (Less et al., 1991), as well as due to geometric resistance (Sevick and Jain, 1989a) (a measure of network irregularities), viscous resistance (Sevick and Jain, 1989b), and RBC mechanical properties (Sevick and Jain, 1991). Jain (1988) summarized basic properties of blood flow within tumors, while data specifically related to transport through capillary walls are given in Jain (1987).

The fundamental process in living organisms represents mass exchange and transport within cells. Cell interior is very complex, composed of different compartments or entities, such as organelles, which are, together with the cell cytoskeleton, immersed into the cell fluid–cytosol (Keener and Sneyd, 2009). Mass transport within cells is a particular branch of biomedical research, and here we cite a few references addressing some aspects of mass transport and exchange. The factors that affect the transport within cells range from biochemical to mechanical to signaling pathways (Rangamani and Iyengar, 2007). Theoretical basis of biochemical processes within different intracellular compartments is formulated (Lauffenburger and Horwitz, 1996; Sun and Pang, 2008; Chu et al., 2013). A computational framework for modeling mass exchange within cells, formulated as a virtual cell, is presented (Schaff et al., 1997; Moraru et al., 2008), which was further used in many applications (Slepchenko et al., 2003).

In electrophysiology, the goal is to determine the electrophysiological properties of all compartments and signal propagation characteristics within the body. For example, in heart electrophysiology, the fundamental advancements were achieved by designing the so-called clamp experiment (Hodkin and Huxley, 1952) in order to determine characteristics of the membrane currents and constitutive relations for the conduction of currents. Following this breakthrough achievement, further important experiments were performed, with modifications and extension of the constitutive relations (Noble, 1962; Baer and Rinzel, 1991; Decker et al., 2009; O'Hara et al., 2011). Based on these experimental results, a large number of computational models related to electrical signal propagation, which includes enormous complexities, have been introduced. For example, model presented (Noble, 1962) includes the role of various transmitting molecules—currents carried by ions through membranes and composite media (Ijiri et al., 2008) include intricate geometry such as in the case of Purkinje network. Since heart is a representative organ with electrical signaling coupled to mechanics, we here refer to a few computational models particularly related to heart modeling and mainly based on the finite element method. A review of computational methods for heart physiology can be found (Clayton and Panfilov, 2008). Among models discussed (Clayton and Panfilov, 2008) is the one related to coupling the electrical field with the mechanical response (Rocha et al., 2011; Lafortune et al., 2012; Dal et al., 2013).

Finally, in this short overview of mass transport and electrophysiology fields of research in science, technology, and

medicine, we note that variation of electrical potential of cell membranes triggers other vital processes within living cells. A typical example is that calcium waves within muscle cells are induced by changes of the membrane potential. Calcium concentration within cells is fundamental for muscle contraction, and various mechanical models for muscles based on the calcium concentration changes are developed (Hunter et al., 1998; Kim et al., 2010; Mijailovich et al., 2010; Lafortune et al., 2012; Santiago, 2018). The variation of electrical potential fields also affects transport of charged particles or drug molecules (Schaff et al., 1997; Trapp and Horobin, 2005), and this kind of mass transport is included in our models (Kojic et al., 2019).

Considering the complexity of computational modeling of physical fields, such as pressure distribution, concentration of various molecules, or field of electrical potential within a body, or even within an organ, it is desirable to have a computational methodology feasible for practical applications. In our previous research, we have introduced a smeared concept for mass transport in capillary system and tissue (Kojic et al., 2017a,b, 2018, 2019; Kojic, 2018; Milosevic et al., 2018a) and demonstrated its superiority with respect to traditional modeling methods.

In this study, we summarize our previously formulated smeared methodology for modeling mass transport in biological tissue and electrophysiology problems and extend it to coupling with muscle mechanics. The motivation for the development of the models, which are applicable to real biomedical problems, is briefly outlined in the text above.

The paper is organized as follows. In the next section, we first summarize the governing equations of the gradient-driven processes: fluid flow through porous media, convective-diffusive particulate transport (including ions) and electrostatics; and then introduce a finite element (FE) form for these governing equations. In Section Smearred Model for Field Problems, the smeared methodology in a general form is summarized (Kojic, 2018), followed by specific forms related the problems described in Section A Summary of the Fundamental Equations for Gradient-Driven Physical Processes and FE Formulation. In Section Coupling Electrophysiology and Muscle Mechanics, we give a short description of coupling the smeared model for electrical potential with muscle mechanics. In Section Representative Results, we present several examples to demonstrate the main features of the smeared concept, including its accuracy and applicability; and, in the final section, we give a short summary and concluding remarks.

A SUMMARY OF THE FUNDAMENTAL EQUATIONS FOR GRADIENT-DRIVEN PHYSICAL PROCESSES AND FE FORMULATION

In this section, we first summarize the gradient-driven problems related to mass transport in blood vessels and tissue and electrophysiology. Then, we present a finite element formulation for these partial differential equations.

Fundamental Equations for the Gradient Driven Field Problems Flow Through Porous Media

In case of incompressible fluid flow through a porous rigid medium, the governing relation is represented by Darcy's law

$$v_i = -k_{Dij} \frac{\partial p}{\partial x_j}, \text{ sum on } j: j = 1, 2, 3 \quad (1)$$

where v_i is the Darcy velocity (as fluid flux per unit area of the continuum) in direction x_i , p is fluid pressure, and k_{Dij} is the Darcy tensor. The mass balance equation is

$$k_{Dij} \frac{\partial^2 p}{\partial x_i \partial x_j} + q_V = 0 \quad (2)$$

WHERE q_V is a source term.

Diffusion

The constitutive law for diffusion is known as Fick's law

$$Q_i = -D_{ij} \frac{\partial c}{\partial x_j} \quad (3)$$

and the mass balance equation is

$$-\frac{\partial c}{\partial t} - v_i \frac{\partial c}{\partial x_i} + \frac{\partial}{\partial x_i} \left(D_{ij} \frac{\partial c}{\partial x_j} \right) + q_V = 0, \quad \text{sum on } i, j: i, j = 1, 2, 3 \quad (4)$$

Here, c is concentration, Q_i flux, and D_{ij} is the diffusion tensor. The generality is kept under the assumption that the diffusion tensor can be a function of concentration, that is, it can be $D_{ij} = D_{ij}(c)$.

Electrostatics

The constitutive law is

$$J_i = -G \frac{\partial V_e}{\partial x_i} \quad (5)$$

where G is electric conductivity, and V_e is electrical potential. The continuity equation for the current density can be derived from Maxwell equations in the form

$$\frac{\partial}{\partial t} \left(\frac{\partial D_i}{\partial x_i} \right) = -\frac{\partial J_i}{\partial x_i}, \text{ sum on } i, i = 1, 2, 3 \quad (6)$$

where the current density components D_i can be related to the potential V_e as

$$D_i = -\varepsilon \frac{\partial V_e}{\partial x_i} \quad (7)$$

where ε is the dielectric constant. Finally, the continuity equation is

$$\varepsilon \frac{\partial}{\partial t} \frac{\partial^2 V_e}{\partial x_i \partial x_i} = -G \frac{\partial^2 V_e}{\partial x_i \partial x_i} + q_V^e \quad (8)$$

where q_V^e is a volumetric source term (coming from ionic transport; Rangamani and Iyengar, 2007).

1D Conditions

For further presentation, we give the expressions for the 1D conditions. For the fluid flow, the 1D conditions follow from the study of flow within pipes (Smith et al., 2002; Canic and Kim, 2003; Kojic et al., 2014). In case of a rigid pipe, the governing equation reduces to

$$k_{pipe} \frac{\partial^2 p}{\partial \bar{x}^2} = 0 \quad (9)$$

where \bar{x} is the pipe direction, and k_{pipe} is the pipe coefficient, which can be derived from the so-called Hagen-Poiseuille law. Additional terms are present in the above equation for the case of deformable pipe (Kojic et al., 2014) but will not be considered in this work.

In case of diffusion, the 1D conditions follow from Equation (4). Hence, we have

$$-\frac{\partial c}{\partial t} - v \frac{\partial c}{\partial \bar{x}} + \frac{\partial}{\partial \bar{x}} \left(D \frac{\partial c}{\partial \bar{x}} \right) + q_V = 0 \quad (10)$$

where \bar{x} is the axis of propagation, and D is diffusion coefficient. In the case of electrical conduction, the governing equation has the form (9) with respect to the electric potential V_e , where instead of k_{pipe} , we have $G_a A$, with A being the neural fiber cross-section.

Transport Through Membranes

Continuum domains of a composite media are often separated by membranes or walls in case of blood vessels or neural fibers. For the presentation of the smeared methodology, we here give the fundamental relations for transport through membranes. In case of fluid flow or diffusion, we have

$$Q_w^p = k_w (p_{in} - p_{out}) \quad (11)$$

$$Q_w^c = D_w (c_{in} - c_{out}) \quad (12)$$

with the flux of fluid Q_w^p and mass due to diffusion Q_w^c oriented outward (from *in* to *out*); k_w and D_w are wall hydraulic permeability and wall diffusivity, respectively. In the case of electrical field, the wall electrical flux relies on the so-called cable theory (Winslow, 1992). The outlet electrical flux (current density) I_m can be expressed as

$$I_m = G_m (V_e^{in} - V_e^{out}) + C_m \left(\frac{\partial V_e^{in}}{\partial t} - \frac{\partial V_e^{out}}{\partial t} \right) \quad (13)$$

where G_m is membrane conductivity, and C_m is specific membrane (wall) capacitance.

Finite Element Formulation

The above governing equations can be transformed into the FE equations of balance for a single finite element by implementing a standard Galerkin weighting method (Kojic et al., 2008). The incremental-iterative form of balance for a time step Δt and iteration i can be derived in the form

$$\left(\frac{1}{\Delta t} \mathbf{M} + \mathbf{K}^v + \mathbf{K} \right)^{(i-1)} \Delta \Phi^{(i)} = \mathbf{Q}^{ext} + \mathbf{Q}^V$$

$$-\frac{1}{\Delta t} \mathbf{M}^{(i-1)} (\Phi^{(i-1)} - \Phi^t) - (\mathbf{K} + \mathbf{K}^v)^{(i-1)} \Phi^{(i-1)} \quad (14)$$

where

$$\begin{aligned} M_{IJ} &= \int_V c_m N_I N_J dV \\ K_{IJ}^v &= \int_V v_i N_I N_{J,i} dV, \text{ sum on } i: i = 1, 2, 3 \\ K_{IJ} &= \int_V D_{km} N_{I,k} N_{J,m} dV, \text{ sum on } k, m: k, m = 1, 2, 3 \\ Q_I^V &= \int_V N_I q_V dV \end{aligned} \quad (15)$$

where Φ stands for pressure, concentration, or electrical potential as nodal variables; N_I are interpolation functions, V is element volume; c_m is mass coefficient ($= 0$ for fluid flow, and $= 1$ for diffusion); D_{km} for fluid is the Darcy tensor, while it is $G\delta_{ij}$ (δ_{ij} is the Kronecker delta symbol) for electrical field. For the case of Darcy's flow or no convection, the convection matrix \mathbf{K}^v is equal to zero. For electrical potential, we have that the "mass" matrix is

$$M_{IJ} = \varepsilon \int_V N_{I,k} N_{J,k} dV, \text{ sum on } k, k = 1, 2, 3 \quad (16)$$

and the convection matrix is equal to zero. Note that for 1D problems, the equations have the same form as the above, with one index k and no summation; and that the element volume is $V = AL$, where A is cross-sectional area and L is the element length. Note that Equation (14) assumes implicit integration scheme over time, that is, all variables are evaluated at the end of time step and at the current equilibrium iteration. This integration scheme is unconditionally stable and provides the best accuracy (Kojic and Bathe, 2005).

For modeling transport through the membranes (walls), we have introduced connectivity 2-node elements for nodes at membranes (Figure 1A) by using double nodes at the same space position at the membrane, with one node belonging to one side and the other to the other side of the boundary between two domains. The balance equation of the form (14) can be applied. The "mass" and transport matrices \mathbf{M} and \mathbf{K} can be written as

$$\begin{aligned} M_{11} &= M_{22} = \frac{1}{3} c_{mm} A_m h_m, \quad M_{12} = M_{21} = \frac{1}{6} c_{mm} A_m h_m \\ K_{11} &= K_{22} = -K_{12} = -K_{21} = D_w A_m \end{aligned} \quad (17)$$

where A_m is the area of the surface belonging to the node, h_m is the membrane thickness; in case of diffusion, D_w is the diffusion coefficient, while instead of D_w , we have k_w and G_m for fluid flow and for electrical conduction, respectively; $c_{mm} = 0$ for fluid flow and $c_{mm} = 1$ for diffusion. For the case of electrical conduction, the non-zero terms of the "mass" matrix are

$$M_{11} = M_{22} = A_m C_m \quad (18)$$

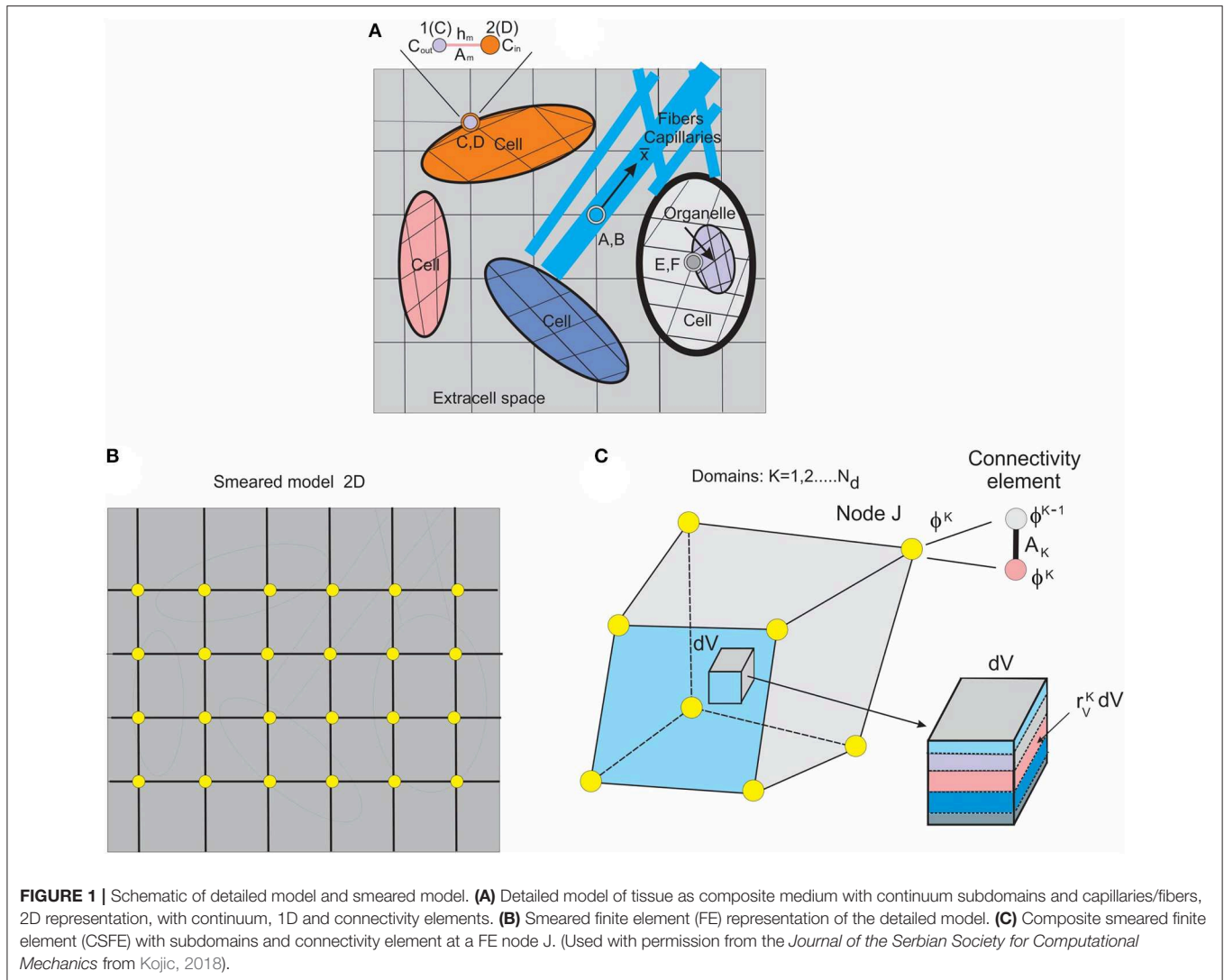


FIGURE 1 | Schematic of detailed model and smeared model. **(A)** Detailed model of tissue as composite medium with continuum subdomains and capillaries/fibers, 2D representation, with continuum, 1D and connectivity elements. **(B)** Smeared finite element (FE) representation of the detailed model. **(C)** Composite smeared finite element (CSFE) with subdomains and connectivity element at a FE node J. (Used with permission from the *Journal of the Serbian Society for Computational Mechanics* from Kojic, 2018).

Finally, in this section, we summarize computational steps related to the incremental-iterative balance Equation (14). The steps are as follows:

1. Loop over time steps

1.1 Loop over equilibrium iterations

- 1.1.1 Loop over finite elements, evaluate, and store into global system element matrices and nodal vectors
- 1.1.2 Solve for the nodal variables
- 1.1.3 Check for the convergence criteria (unbalanced vector on the right-hand side are small and/or increments of nodal variables are small).
If the convergence criteria are not satisfied, update the solution and go to next equilibrium iteration
- 1.2.1 If convergence criteria are satisfied, store solution and go to the next time step 1.

END OF SOLUTION.

SMEARED MODEL FOR FIELD PROBLEMS

To introduce the smeared methodology (Kojic et al., 2014), we first consider a detailed model of a composite medium. A schematic of a medium composed of continuum domains-compartments together with a network of fiber-like 1D domain is shown in **Figure 1A**. The continuum domains include extracellular space, cells, and organelles. Capillaries and lymph vessels, and neural fibers, are represented by 1D elements within extracellular space, while cells can contain organelles—hence, the continuum domains have a hierarchical character. Each domain has its own FE mesh of continuum elements, while 1D domains have their own 1D finite elements with the coordinate axes along the elements (\bar{x} axis depicted at one of these fibers).

Connectivity elements are shown as A, B; C, D; E, F; and enlarged at the top of the **Figure 1A** (the nodes C, D, also denoted as 1, 2). The two nodes, 1 and 2, have nodal values representing the two domains (ϕ_{out} and ϕ_{in} in the figure). The characteristics

of the connectivity elements assigned to the boundary common nodes are membrane (or wall) transport coefficient, cross-section area A_m , and the membrane (wall) thickness h_m .

It can be seen from the detailed model description that significant effort is required to generate the model. The model generation would be an impractical or even impossible task in case of a complex medium such as tissue. In case of employing continuum FEs for membranes instead of connectivity elements, this task would be more demanding.

To overcome complexity issues, we further introduce a smeared model by formulating a continuum composite finite element (CSFE). The CSFE includes all constituents (continuum and 1D) in a way that the true physical fields, corresponding to a detailed model, are represented in a kind of average, so-called "smeared" sense, providing adequate accuracy. The smeared model for the same detailed model of **Figure 1A**, and with continuum elements only, is schematically shown in **Figure 1B**.

A few conceptual steps need to be considered to formulate the CSFE element. First, the 1D balance equations are necessary to be transformed into the corresponding continuum format. The derivations of the continuum transport tensor, for a general physical field, are given (Kojic, 2018) and can be expressed as

$$D_{ij} = \frac{1}{A_{tot}} \sum_K D_K A_K \ell_{K_i} \ell_{K_j} \quad (19)$$

where A_{tot} is the total area of 1D domains in a reference volume; A_K is cross-sectional area of element K ; D_K and ℓ_{K_i} are transport coefficients along the 1D elements and directional coefficients, respectively.

Each domain in the CSFE formulation has its own field within the corresponding volume of the CSFE. Therefore, as shown in **Figure 1C**, the FE node of the CSFE has a number of degrees of freedom ϕ^K equal to the number of domains N_d . The domain volume V_K can be expressed as

$$V_K = r_V^K V, \text{ and } dV_K = r_V^K dV \quad (20)$$

where r_V^K is the volumetric fraction, and V is the total element volume.

Corresponding domains are coupled using connectivity elements placed at each node of the CSFE and in accordance to previously described connectivity elements in the detailed model. The cross-sectional area A_{JK} of a connectivity element at node J for the domain K can be expressed in the form

$$A_{JK} = (r_{AV}^K V_K)_J = (r_{AV}^K r_V^K V)_J \quad (21)$$

where r_{AV}^K is the area coefficient expressed as $r_{AV}^K = A_K/V_K$, and V_J is the volume of the total space of the continuum belonging to the node J . This volume can be evaluated as

$$V_J = \sum_{el} \int_{V_{el}} N_J dV_{el} \quad (22)$$

where summation el goes over all finite elements with the common node J . Note that for convenience of modeling of any non-homogenous property of the material system, all of the

surfaces, volumes, and volumetric and area ratios are assigned to FE nodes.

The finite element balance equations for continuum and connectivity elements are of the same form as in detailed model (Equation 14) with the matrices

$$\begin{aligned} M_{IJ} &= \int_V c_m N_I N_J r_V^K dV \\ K_{IJ} &= \int_V D_{ij} N_{I,i} N_{J,j} r_V^K dV, \quad \text{sum on } i, j: i, j = 1, 2, 3 \quad (23) \\ Q_I^V &= \int_V N_I q_V r_V^K dV \end{aligned}$$

where the material parameters are as in Equation (15). In case of electrical field, the matrix \mathbf{M} in Equation (16) is now

$$M_{IJ} = \varepsilon \int_V N_{I,k} N_{J,k} r_V^K dV, \quad \text{sum on } k, k = 1, 2, 3 \quad (24)$$

and the source nodal vector due to ionic transport of a molecule m is (Kojic et al., 2019)

$$Q_I^{mE} = \frac{DFz^m}{RT} \int_V N_I \frac{\partial}{\partial x_i} \left(c^m \frac{\partial V_e}{\partial x_i} \right) r_V^K dV \quad (25)$$

where D is diffusion coefficient, z^m is the molecule valence, F is the Faraday constant, R is the gas constant, T is absolute temperature, and c^m is concentration. The surface areas entering into matrices of the connectivity elements are as given in Equation (21).

The above concept has been implemented for diffusion and fluid transport through complex systems consisting of capillary network and tissue, with inclusion of the hydrophobicity effects in the connectivity elements (Kojic et al., 2014, 2017a, 2018), and with improvements of accuracy of the smeared methodology achieved by the correction function introduced in Milosevic et al. (2018a). The robustness and applicability of the smeared model are demonstrated (Milosevic et al., 2018b), where the CSFE is extended for modeling drug release from a complex mesh of drug-loaded nanofibers.

COUPLING ELECTROPHYSIOLOGY AND MUSCLE MECHANICS

Muscles (here assumed skeletal muscles) in the body are activated by electrical signals transmitted from the central nervous system to muscle cells. The signals trigger muscle activation since they produce a change in the cell membrane potentials, which further leads to flow through membrane of ions vital for cell functioning, such as potassium, sodium, calcium, and others (Hodkin and Huxley, 1952; Noble, 1962; O'Hara et al., 2011). The ion flow is bidirectional through various biological mechanisms. There are a number of mathematical models that connect the membrane potential change with activation of muscles. For example, for cardiac muscle, the mathematical expressions for generation of

the so-called active stress along the muscle fiber, which produces the muscle contractile force, the membrane potential is used directly (Dal et al., 2013) or through the concentration of calcium Ca^{2+} within the muscle cell (Hunter et al., 1998; Lafortune et al., 2012; Berberoglu et al., 2014). The calcium Ca^{2+} is the crucial molecule that catalyzes the biochemical cycle of conformational change of muscle fiber molecules and therefore transformation of chemical into mechanical energy. Hence, in modeling muscle mechanical action, it is necessary for these models to have the calcium concentration change within muscle cells over time. We will use a widely accepted relation (Hunter et al., 1998)

$$\sigma_{act} = \frac{[Ca^{2+}]^n}{[Ca^{2+}]^n + C_{50}^n} \sigma_{max} [1 + \eta (\lambda - 1)] \quad (26)$$

where σ_{act} is the active stress along the fiber, Ca^{2+} is calcium concentration, σ_{max} is maximum isometric stress, C_{50} is concentration for 50% availability of actin sites for the crossbridge binding, n is related to the rate of this availability to concentration, η is parameter that is governing the rate of muscle fiber deformation, and λ is the fiber stretch.

Computational models of skeletal muscles and their implementation to the physiological conditions have been the subject of intensive research within the computational community (e.g., Kojic et al., 1998; Stojanovic et al., 2007; Mijailovich et al., 2010, and references therein).

We use velocity formulation, that is, the nodal variables are velocities—convenient to couple solid and fluid mechanics (Isailovic et al., 2014; Kojić et al., 2015), while stresses in solids are calculated from strains or stretches. The balance equation of a finite element can be written in the form (Kojic et al., 2008)

$$\left(\frac{1}{\Delta t} \mathbf{M} + \Delta t \mathbf{K} \right) \Delta \mathbf{V}^{(i)} = \mathbf{F}^{ext} - \mathbf{F}^{int(i-1)} - \frac{1}{\Delta t} \mathbf{M} (\mathbf{V}^{(i-1)} - \mathbf{V}^t) \quad (27)$$

where the mass and stiffness matrices \mathbf{M} and \mathbf{K} have a standard form (Kojic et al., 2008), and \mathbf{V} and \mathbf{V}^t are nodal velocities at the current (or previous) iteration and at start of time step, respectively; \mathbf{F}^{ext} and \mathbf{F}^{int} are external and internal nodal forces; nodal variables are one-dimensional arrays. Specific to muscle deformation is that, besides the material stress dependent on the state of deformation, there exists the active stress σ_{act} entering into the internal force vector as noted above.

REPRESENTATIVE RESULTS

We have selected two numerical examples to illustrate the main characteristics of our smeared modeling methodology. The first example shows applicability of smeared models to large biological systems; here, a liver with two tumors is modeled. In the second example, accuracy of solutions is investigated on a small sample of the heart wall tissue, including coupling between electrophysiology and mechanics. The models are built into our FE code PAK (Kojic et al., 2010) with the corresponding CAD interface developed at R&D Center for Bioengineering BIOIRC.

We prepared animations for both examples, which are given in **Supplementary Material**.

Liver Model With Tumors—Application of the CSFE

Liver model is based on geometry used (Kojic et al., 2017b), with two additional spheres modeled to mimic two tumor

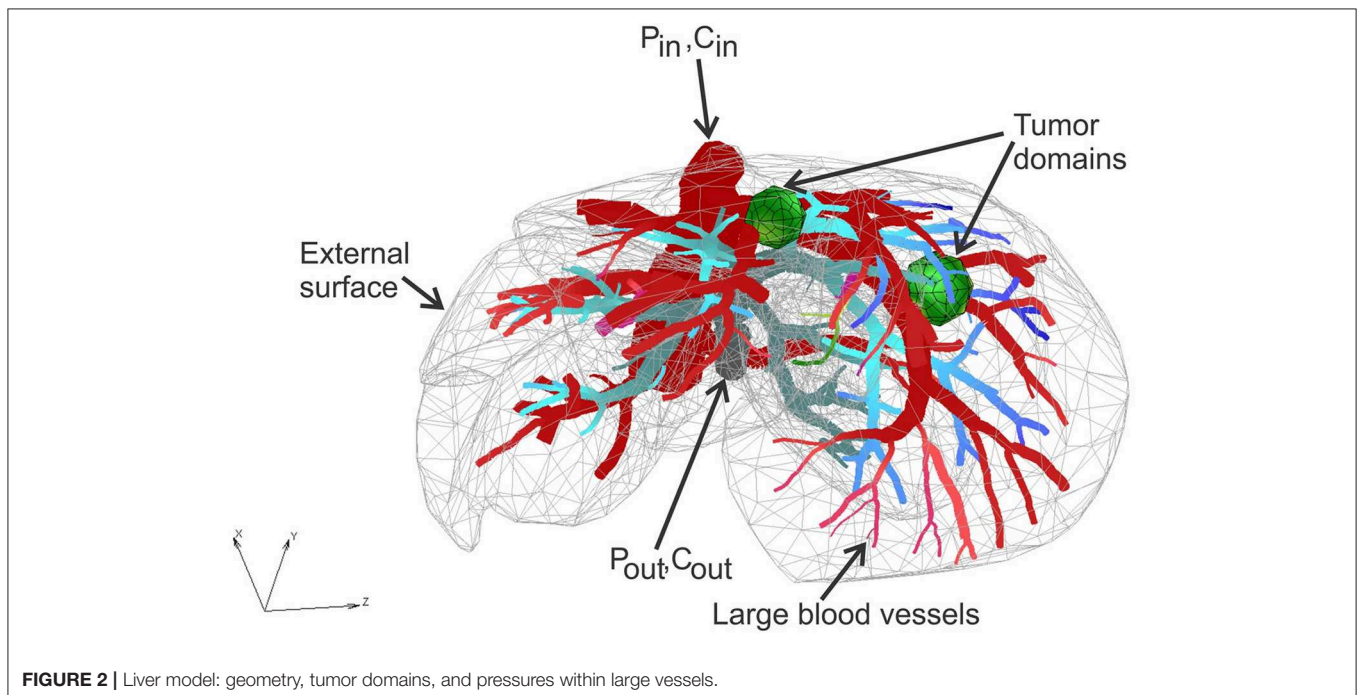


FIGURE 2 | Liver model: geometry, tumor domains, and pressures within large vessels.

domains. Micro computed tomography (micro-CT) was used by the Preclinical Imaging Core at the Houston Methodist Research Institute to scan the vascular structure of a mouse liver. The geometry of the liver and blood vessel network is generated from micro-CT scan using procedure presented (Zagorchev et al., 2010). The geometry of the model is shown in **Figure 2**.

The FE model consists of 39,832 3D CSFEs, 7,736 1D pipe FEs for larger vessels, 726 connectivity elements for connecting large vessels with continuum nodes of smeared FEs. Two separate tumors within liver are with a total of 316 3D FE elements. The total number of nodes is 54,590. Data for this example are the same as in Kojic et al. (2017b).

Prescribed conditions in larger vessels (at input/output nodes of 1D pipe elements mesh) are: Inlet Pressure is 3,999.7 Pa (30 mmHg), Outlet Pressure is 1,333.2 Pa (10 mmHg), Inlet Concentration is bolus type $c(t)$, presented in **Figure 6**, and outlet concentration is set to be 0.

Characteristics of fluid/diffusion flow through blood vessels (large vessels and capillaries) are: viscosity is 10^{-3} Pa s, and diffusion coefficient is $1,000 \text{ mm}^2/\text{s}$.

Characteristics of blood vessel walls are: hydraulic permeability coefficient is $10^{-12} \text{ mm}/(\text{Pa s})$, diffusion coefficient is $0.1 \text{ mm}^2/\text{s}$, and thickness is 10% of the vessel diameter.

Characteristics of tissue are: diffusion coefficient is $0.1 \text{ mm}^2/\text{s}$, and Darcy coefficient is $10^{-12} \text{ mm}^2/(\text{Pa s})$.

Parameters of smeared model are: average capillary diameter is 0.025 mm, capillary wall thickness is 0.0025 mm, volume fraction is 10%, diffusion coefficient of capillary wall is $10^{-6} \text{ mm}^2/\text{s}$, and hydraulic permeability of capillary wall is $10^{-12} \text{ mm}/(\text{Pa s})$. The adopted values of material and geometric parameters are according to literature data, for example, Rushmer (1976), Gerlowski and Jain (1986), Jain (1988), Keener and Sneyd (2009).

Time steps used in simulations are: $40 \times 2.5 \text{ s}$.

Additionally, there are two tumors in the model with the following characteristics:

	Tumor 1	Tumor 2
Diff. coeff in extracellular space [mm^2/s]	100	10
Darcy coefficient [$\text{mm}^2/(\text{Pa s})$]	1	0.1
Hydraulic coefficient [$\text{mm}/(\text{Pa s})$]	1	0.1
Diffusion coefficient in small capillaries [mm^2/s]	100	10
Diff. coeff of capillary wall [mm^2/s]	100	10
Partitioning of capillary wall	0.8	0.7
Diff. coeff within cells [mm^2/s]	100	100
Diff. coeff of cell membrane [mm^2/s]	100	100

As can be seen from these data, we assumed 10 times smaller diffusion coefficient within tumor 2 than in tumor 1 to show the difference in concentration between these tumors.

With these material data and boundary conditions, we have solved for pressures and concentrations within the liver and two tumors using our smeared methodology. Some of the results are summarized below.

Pressure fields for two views of the model are shown in **Figure 3** for the outer surface of 3D smeared elements, cross-section, and a dotted representation of large vessels and continuum. Tumor surfaces are indicated by dashed lines. As can be seen from this figure, there is evident reduction in pressures, starting from large vessels to capillaries and further to tumors and healthy tissue.

Vectors of velocities, field of velocity on the outer surface with a clipping plane, and vectors of velocities within tumors, for two different views on the model, are shown in **Figure 4**. For one of the tumors, T1, there is a positive pressure difference with respect to the surrounding tissue, which induces velocity vectors pointing out of tumor, that is, fluid is flowing out of tumor (**Figure 4C-T1**).

The concentration field within large vessels, liver tissue, and tumors is shown in **Figure 5** for three time points. The largest values of the concentrations are noticeable in blood vessels, following a decrease going to capillaries and tissue. Also, concentration within tumor T2 is smaller compared to that of tumor T1 due to reduced diffusion coefficients.

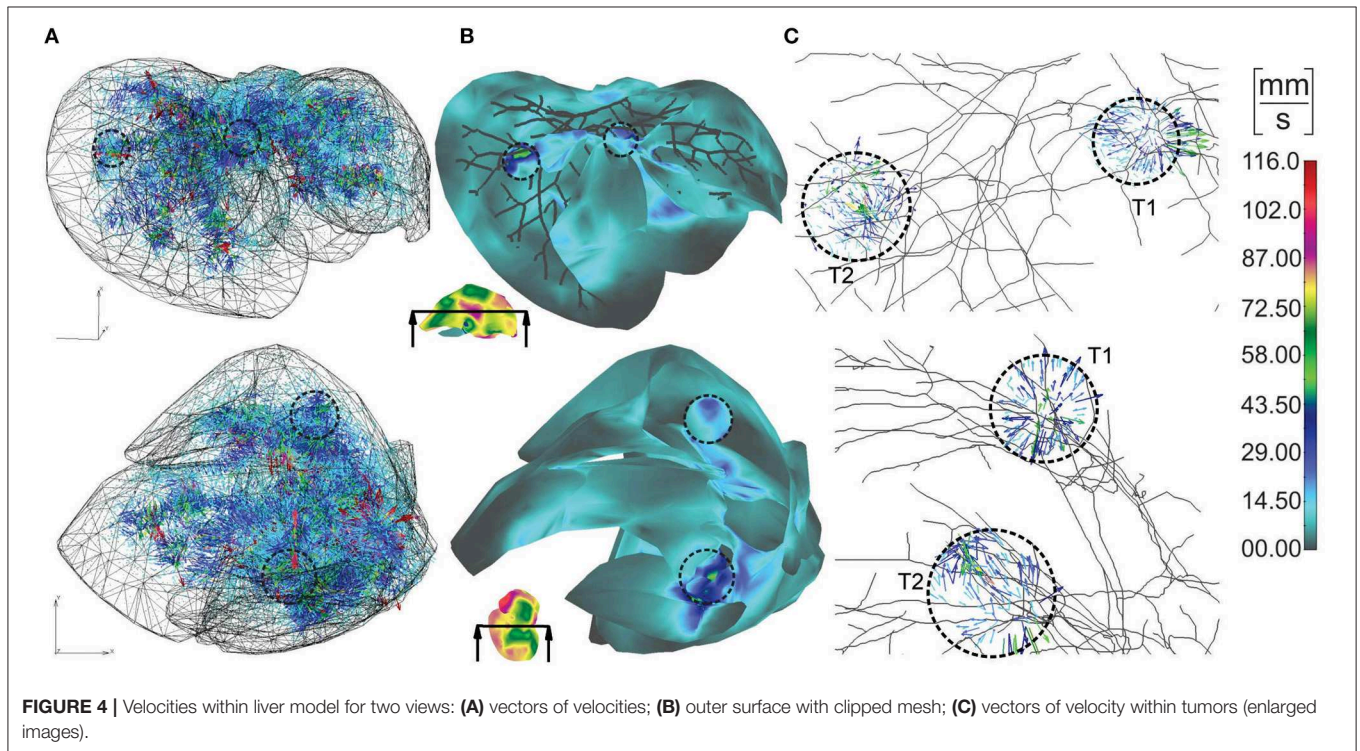
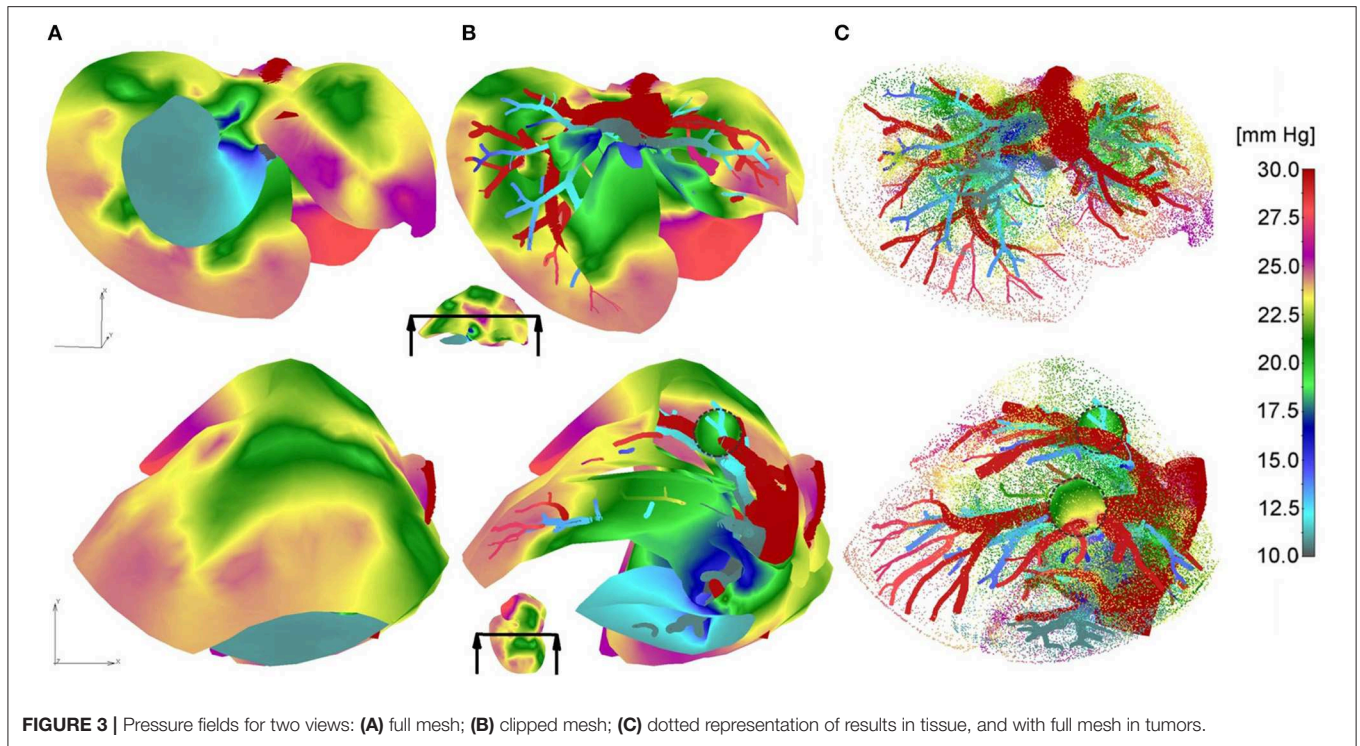
Change of the mean concentration within capillaries, tissue of liver, and tumors T1 and T2, is shown in **Figure 6**. In the first period of the process of drug transport within the liver, concentration within capillaries, tissue, and tumors is increasing according to increase of the entering mass (concentration). The concentration within capillaries reaches maximum with respect to the maximum of the entering $c(t)$, which is also the case for tissue and tumor domains. It is evident that concentration in tumor T1 is higher than in tumor T2 due to the larger diffusion and partitioning coefficients.

Electrophysiological and Mechanical Model of the Heart Wall

To investigate accuracy of our CSFE model, a small sample of heart wall tissue is selected (**Figure 7**) following data (Blausen Medical, 2014; Santiago, 2018). From this model, we extract the first layer of muscle cells in myocardium, which is close to the sub-endocardium: the domain that includes the Purkinje fibers.

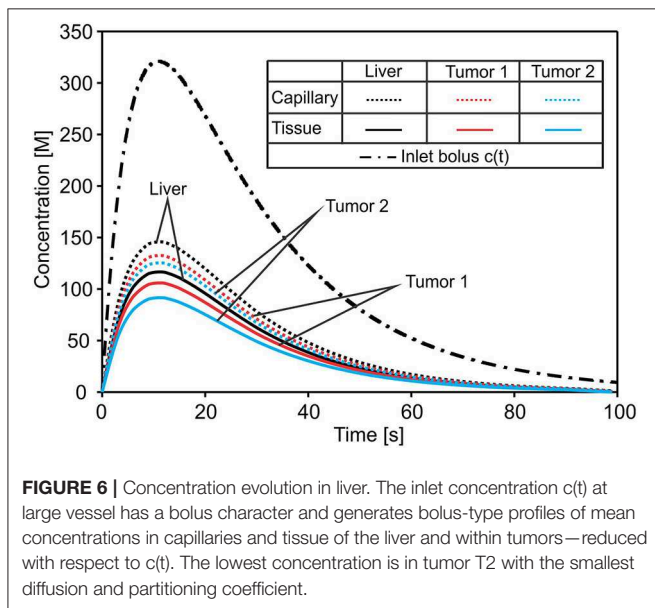
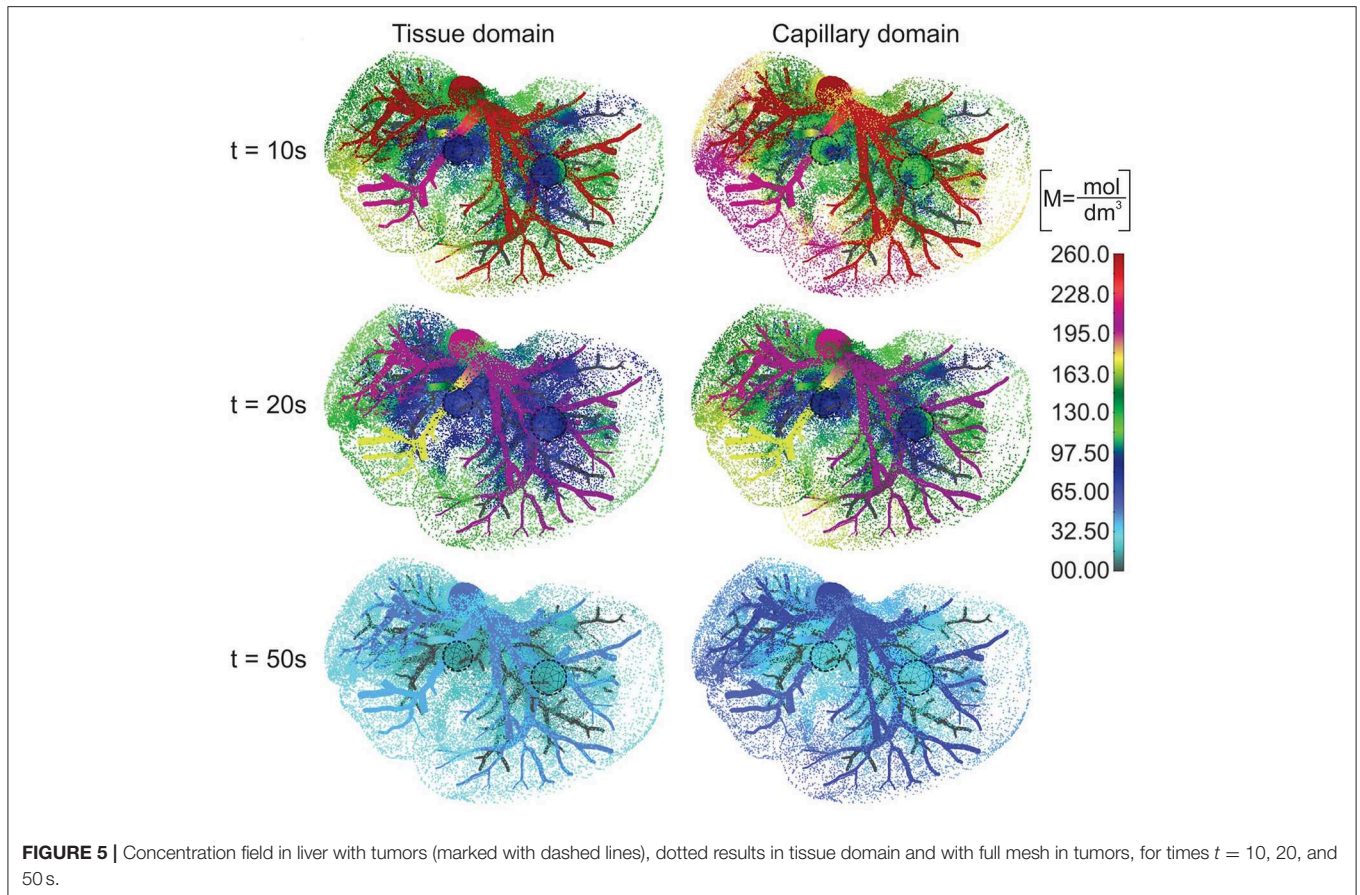
According to the image in **Figure 7** (right panel), the detailed 2D model is generated (**Figure 8A**), which consists of the mesh of 1D Purkinje fibers and 25 cells. Dimension of the model is $230 \times 150 \mu\text{m}$, volume fraction of cells is $r_V = 0.71$, and area/volume ratio of cell is $r_{AV} = 0.18$. Based on the detailed model, we generated the smeared model (**Figure 8B**) for calculation of the electrical potential and calcium current and concentration (O'Hara et al., 2011). FE nodes of 1D Purkinje fibers are connected with 2D FE nodes of extracellular space domain using connective 1D elements. As shown in **Figure 8**, it is assumed that the left vertical boundary of the tissue is constrained to displacements in x direction, and lower horizontal boundary is constrained to displacements in y direction. We assumed that muscle fibers have longitudinal direction with respect to the muscle cells, that is, they are aligned to the x direction.

Data used in the model are: electric conductance (G_i , $I = x, y, z$) of extracellular space (further called tissue), cells, and in neural



fibers is $1,000 [AV^{-1}m^{-1}]$; specific membrane conductance (C_m) of Purkinje fibers is $1,000 [S/\mu m^2]$; specific membrane capacitance of Purkinje fiber's membrane and cell membrane

is $1,000 [AsV^{-1}\mu m^{-2}]$, and $G_m = 0$ for the fiber membrane. Diffusion coefficient of Ca^{2+} for tissue and cell is assumed to be $1,000 [\mu m^2/s]$, while it is assumed that there is no diffusive



The function of the electric potential is taken from Noble (1962): it consists of two identical cycles and is prescribed at inlet nodes of the Purkinje mesh [$V_e(t)$ in **Figure 8**]. We assumed constant potential inside cells ($V_e = -20$ mV). Accumulated current density (I_{ORd}) in cell membrane is calculated according to ORD model (O’Hara et al., 2011) and added to Equation (13) of the FE solution procedure. For these conditions, change of the mean electric potential within tissue is shown in **Figure 9A**. Results are almost identical for both detailed and smearred models. Currents of ORD model that affect concentration of the Ca^{2+} in myoplasmic compartment are: $I_{pCa}, I_{Cab},$ and $I_{NaCa,i}$; while currents that affect concentration of Ca^{2+} in the subspace compartment are I_{CaL} and $I_{NaCa,ss}$. Mean current density I_{Ca} for transport of the Ca^{2+} ions can be calculated as (O’Hara et al., 2011):

$$I_{Ca} = - \left(I_{pCa} + I_{Cab} - 2 \cdot I_{NaCa,i} \right) \frac{V_{myo}}{V_{myo} + V_{ss}} - \left(I_{CaL} - 2 \cdot I_{NaCa,ss} \right) \frac{V_{ss}}{V_{myo} + V_{ss}} \quad (28)$$

transport through cell membrane. Material parameters of the muscle mechanical model (Equation 28), used in this example, are: $n = 0.4, C_{50}^n = 0.5, \eta = 0.2,$ and $\sigma_{max} = 100$ kPa.

where V_{myo} and V_{ss} are volumes of the myoplasmic compartment and subspace compartment, respectively. Change with time of the mean current density obtained by using detailed and smearred

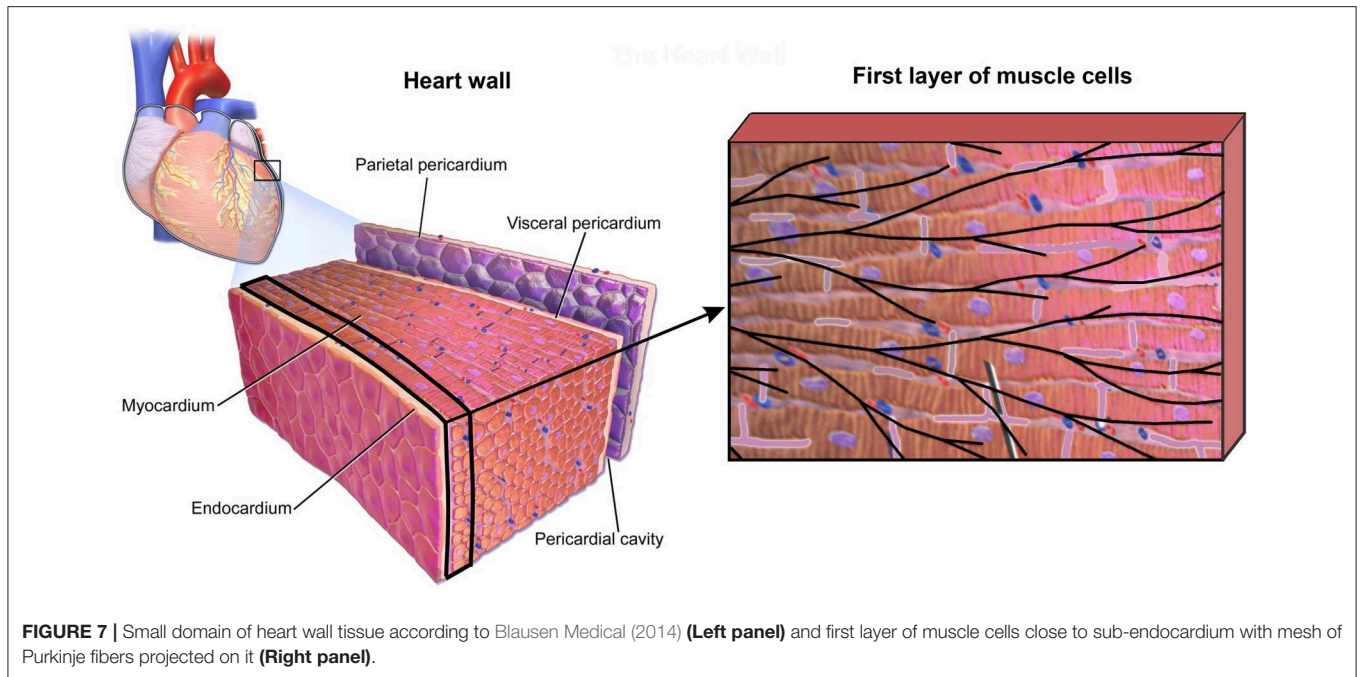


FIGURE 7 | Small domain of heart wall tissue according to Blaussen Medical (2014) (**Left panel**) and first layer of muscle cells close to sub-endocardium with mesh of Purkinje fibers projected on it (**Right panel**).

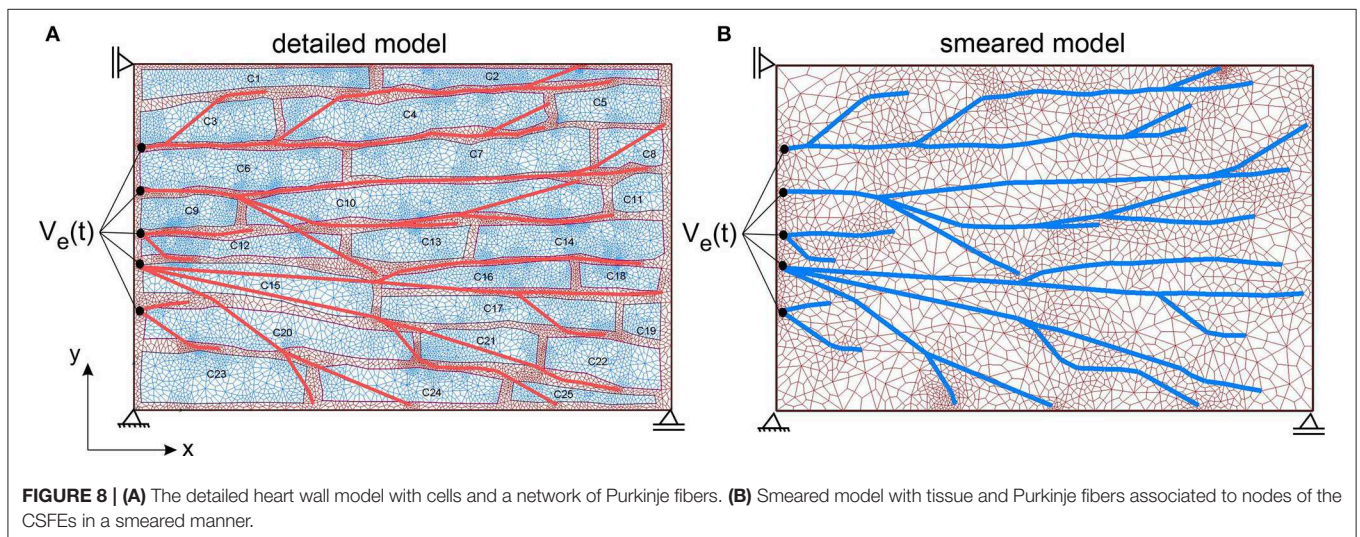


FIGURE 8 | (A) The detailed heart wall model with cells and a network of Purkinje fibers. **(B)** Smeared model with tissue and Purkinje fibers associated to nodes of the CSFEs in a smeared manner.

model is shown in **Figure 9B**, where I_{ca} for the detailed model is calculated as average over all cells.

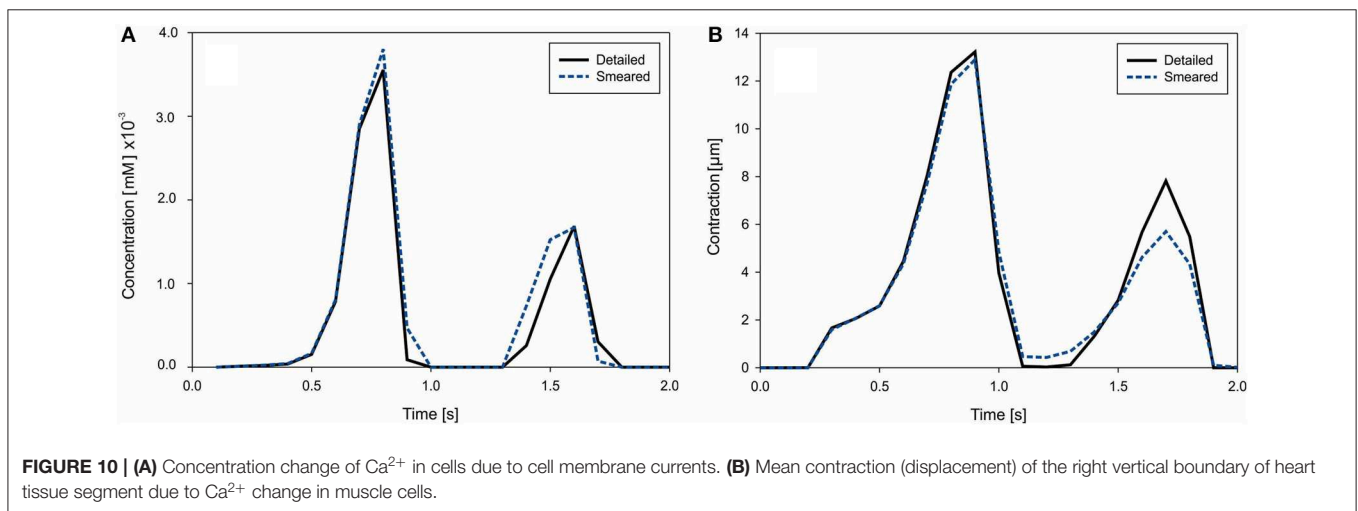
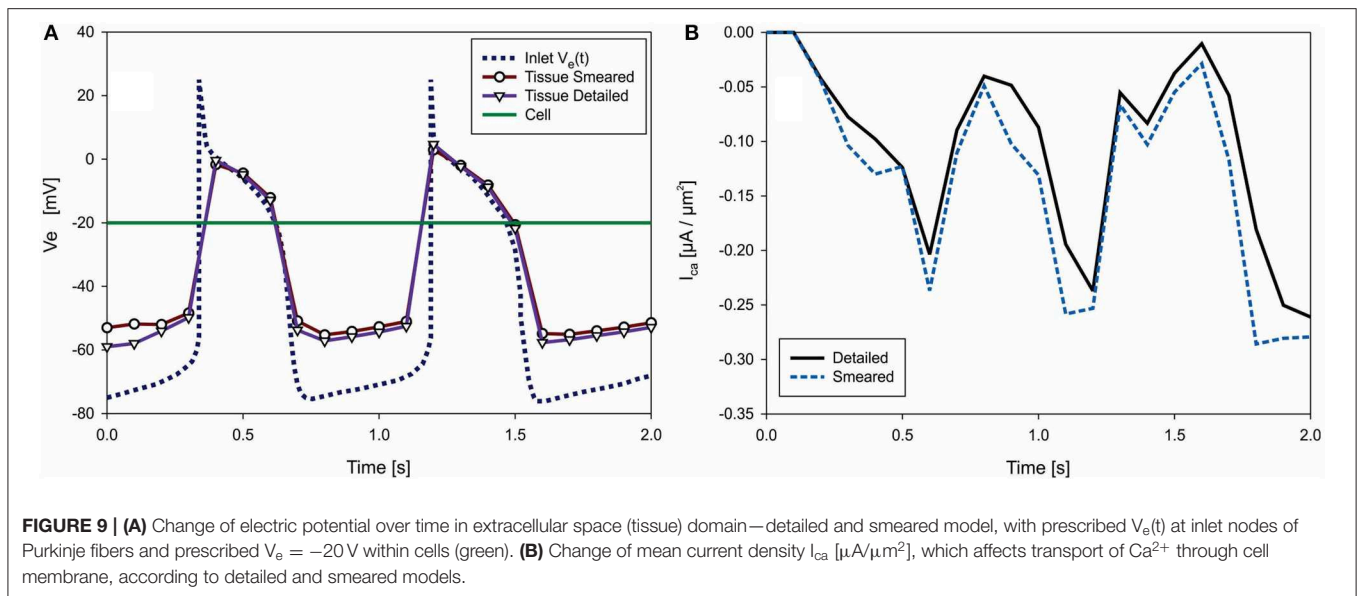
Mean concentration in cells, $[Ca^{2+}]_{mean}$, is calculated as average concentration in cells composed of myoplasmic (denoted by index “i”), subspace (“ss”), network SR (“nsr”), and junctional SR (“jsr”) compartments, according to O’Hara et al. (2011)

$$\begin{aligned}
 [Ca^{2+}]_{mean} = & ([Ca^{2+}]_i \cdot V_{myo} + [Ca^{2+}]_{ss} \cdot V_{ss} \\
 & + [Ca^{2+}]_{nsr} \cdot V_{nsr} + [Ca^{2+}]_{jsr} \cdot V_{jsr}) / V_{cell}
 \end{aligned}
 \tag{29}$$

where $V_{myo} = 0.68 V_{cell}$, $V_{ss} = 0.02 V_{cell}$, $V_{nsr} = 0.0552 V_{cell}$, and $V_{jsr} = 0.048 V_{cell}$. Concentrations of Ca^{2+} in each

compartment (*i*, *ss*, *nsr* and *jsr*) of ORD model are calculated according to equations provided in Supplementary of Reference (O’Hara et al., 2011). Change of the mean concentration within cells (cell domain), for both detailed and smeared models, is shown in **Figure 10A**.

Muscle contraction occurs from the generation of active stress according to Equation (26), where concentration of calcium is evaluated by our transport models (detailed and smeared). The mechanical response is calculated using the equation of motion (27). Mean contraction (displacement) of the right vertical tissue boundary is shown in **Figure 10B**. The largest contractions occur at $t = 0.9s$ and $1.6s$, which are in accordance with the Ca^{2+} concentration within cells.



Effective contraction (modulus of the displacement vector) field of the tissue for the first cycle of action potential function $V_e(t)$ is shown in **Figure 11**. It can be seen that the largest contraction occurs at $t = 0.9\text{s}$. Good agreement is observed between the results of the two models.

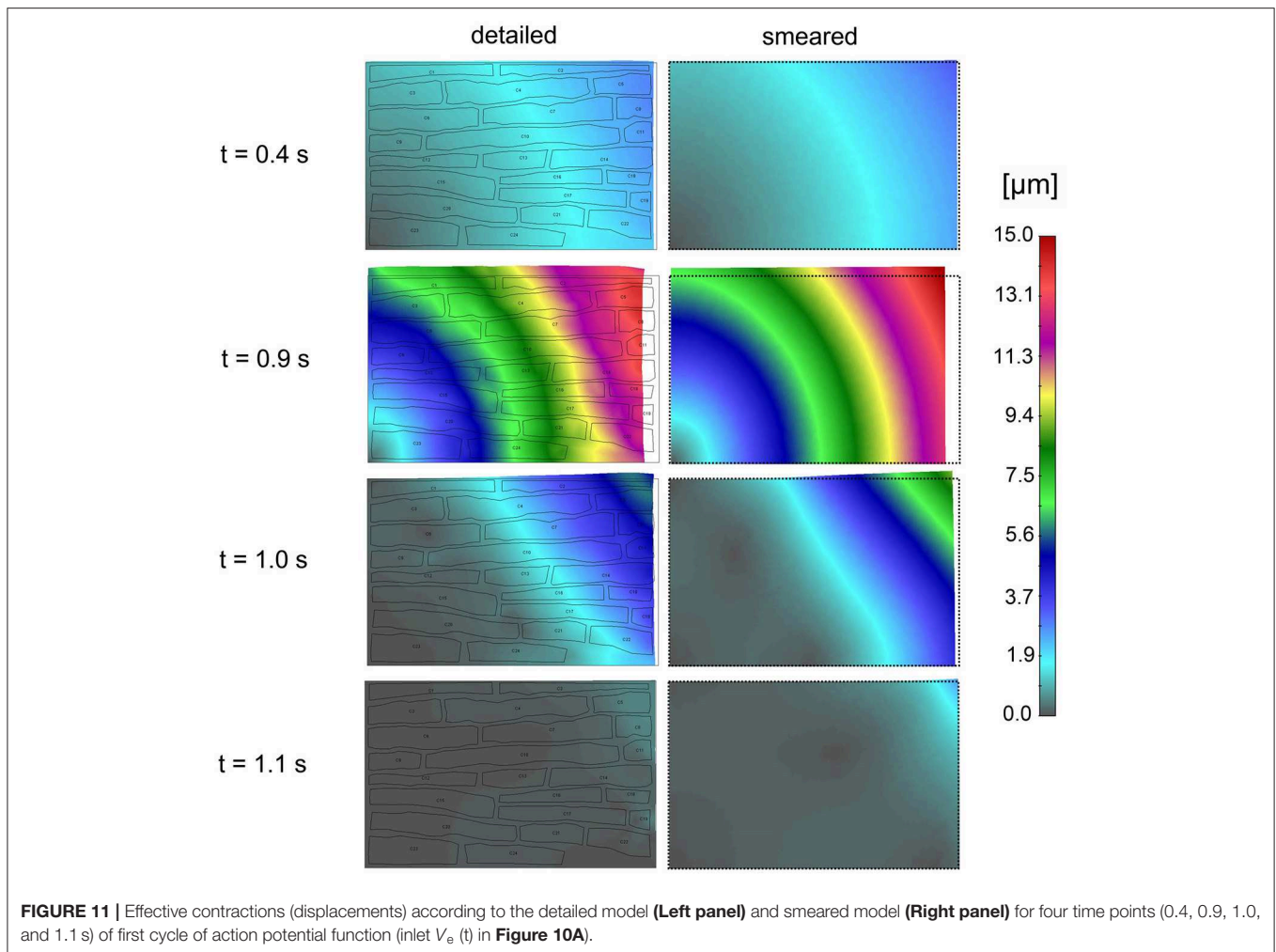
Electric field potentials within extracellular space for four time points, according to detailed and smeared model, are shown in **Figure 12**. Potential within cells is kept constant $V_e = -20\text{mV}$. Agreement between solutions of the two models is noted.

DISCUSSION

The main aims of the study were first to demonstrate applicability of our previously published general smeared finite element formulation for the physical fields to large-scale biological

problems and second to include electromechanical coupling as the fundamental process for the muscle activation.

Considering the first aim, we note that, by using the today available computational models, software, and hardware, it is practically impossible to calculate drug distribution within an entire organ with different scales, from macro- to nano-, and modeling in detail blood vessels, cells, extracellular space, and even cell interior. On the contrary, our smeared FE methodology offers a platform to achieve solutions for this multiscale problem. We have selected for demonstration a liver of a mouse and generated continuum model with the geometry obtained from images. The model is simple since it consists of 3D continuum finite elements, with the 1D FEs for larger blood vessels as the only addition. The model, for the sake of generality, includes two tumors with different transport properties. The transport parameters data, including hydraulic and diffusive components, are taken according to available references (Gerlowski and Jain,



1986; Sevick and Jain, 1989b, 1991; Less et al., 1991; Mathura et al., 2001; Hall, 2016). The results displayed here show the concentration field, pressure distribution, and fluid velocities in different domains that are quantitatively correct. Accuracy of the solutions can be examined by, first of all, comparison with experiments. Comparison with other available numerical solutions in literature, such as those related to one domain only (e.g., tumor), would be possible with imposing the appropriate boundary conditions in our smeared model. This is not done here, since accuracy of our smeared models was examined in detail in our previous references (Kojic et al., 2017a,b, 2018, 2019; Milosevic et al., 2018b).

Detailed comparison of the smeared models in electrophysiology with the traditional models is given (Kojic et al., 2019). It was found in that analysis that the smeared model is advantageous with respect to the traditional monodomain and bidomain models (e.g., Roth and Wikswo, 1986; Henriquez, 1993; Henriquez et al., 1996; Keener and Panfilov, 1996) (reviewed in Clayton and Panfilov, 2008; Clayton et al., 2011). The deficiency of the traditional models also is that they do not include volumetric fractions of the distinct domains, which obviously must affect the solution. On the other

hand, our smeared model relies on the multiple continuum domains coupled by the appropriate connectivity elements. Furthermore, smeared models are simple for application as, for example, in case of the heart: instead to model in detail neural fibers, the entire His-Purkinje system of the heart (Vigmond and Stuyvers, 2016) can be modeled by using the conductivity tensor of the form (19) within continuum 3D finite elements.

With the field of electrical potential within Purkinje network, extracellular and cell interior domain, coupled by the connectivity elements, it is possible to calculate membrane potential that governs the change of the calcium concentration within muscle cells according to Equation (29). It is further straightforward to compute the active stress within muscle cells by employing Equation (26), as one of the commonly used relationships.

CONCLUDING REMARKS

The presented smeared finite element formulation offers a platform for multiscale modeling of physical field within a

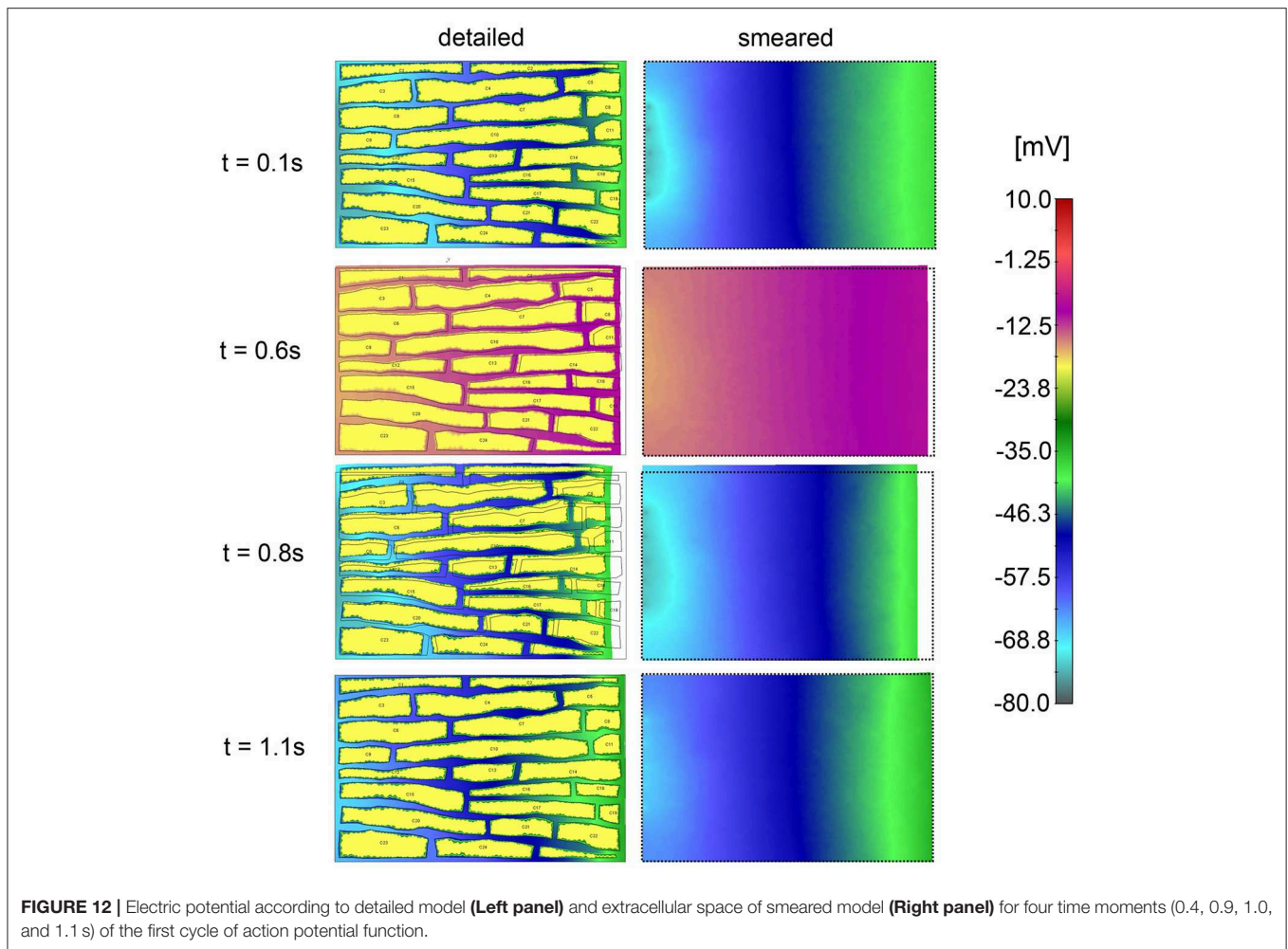


FIGURE 12 | Electric potential according to detailed model (**Left panel**) and extracellular space of smeared model (**Right panel**) for four time moments (0.4, 0.9, 1.0, and 1.1 s) of the first cycle of action potential function.

complex medium. Being simple for application, it is suitable for modeling large biological systems, such as liver with tumors used as an example in this study. It is straightforward to implement this approach to other organs, as lung, heart, pancreas, and so on and even brain. The brain has additional complexities related to signal transmission, but the presented model of the Purkinje network and electrical field within tissue shows that a brain model can be developed. The demonstrated electromechanical coupling demonstrates that this methodology can be implemented to muscle modeling in general.

DATA AVAILABILITY STATEMENT

All datasets generated for this study are included in the article/**Supplementary Material**.

AUTHOR CONTRIBUTIONS

MK formulated the methodology. MM designed the examples and analyzed results. VS, BM, and VG performed the numerical simulations and prepared results. SN, AZ, NF, and MF

provided the data and images for reconstructing the liver and electrophysiology examples.

FUNDING

This work was supported by the SILICOFM project that has received funding from the European Union's Horizon 2020 research and innovation programme under grant agreement No. 777204.

ACKNOWLEDGMENTS

The authors acknowledge support from the City of Kragujevac, Serbia, Ministry of Education and Science of Serbia (Grants OI 174028 and III 41007), and also from National Cancer Institute under grant U54 CA210187.

SUPPLEMENTARY MATERIAL

The Supplementary Material for this article can be found online at: <https://www.frontiersin.org/articles/10.3389/fbioe.2019.00381/full#supplementary-material>

REFERENCES

- Baer, S. M., and Rinzel, J. (1991). Propagation of dendritic spikes mediated by excitable spines: a continuum theory. *J. Neurophysiol.* 65, 874–890. doi: 10.1152/jn.1991.65.4.874
- Berberoglu, E., Solmaz, H. O., and Göktepe, S. (2014). Computational modeling of coupled cardiac electromechanics incorporating cardiac dysfunctions. *Eur. J. Mech. Solids* 48, 60–73. doi: 10.1016/j.euromechsol.2014.02.021
- Blanco, E., Shen, H., and Ferrari, M. (2015). Principles of nanoparticle design for overcoming biological barriers to drug delivery. *Nat. Biotechnol.* 33, 941–951. doi: 10.1038/nbt.3330
- Blausen Medical (2014). Medical gallery of Blausen Medical 2014. *Wikif. Med.* 1:10. doi: 10.15347/wjm/2014.010
- Canic, S., and Kim, E. H. (2003). Mathematical analysis of the quasilinear effects in a hyperbolic model blood flow through compliant axis-symmetric vessels. *Math. Meth. Appl. Sci.* 26, 1161–1186. doi: 10.1002/mma.407
- Chu, X., Korzekwa, K., Elsbey, R., Fenner, K., Galetin, A., Lai, Y., et al. (2013). Intracellular drug concentrations and transporters: measurement, modeling, and implications for the liver. *Clin. Pharmacol. Ther.* 94, 126–141. doi: 10.1038/clpt.2013.78
- Cinar, Y., Demir, G., Paç, M., and Cinar, A. B. (1999). Effect of hematocrit on blood pressure via hyperviscosity. *Am. J. Hypertens.* 12, 739–743. doi: 10.1016/S0895-7061(99)00011-4
- Clayton, R. H., Bernus, O., Cherry, E. M., Dierckx, H., Fenton, F. H., Mirabella, L., et al. (2011). Models of cardiac tissue electrophysiology: progress, challenges and open questions. *Prog. Biophys. Mol. Biol.* 104, 22–48. doi: 10.1016/j.pbiomolbio.2010.05.008
- Clayton, R. H., and Panfilov, A. V. (2008). A guide to modelling cardiac electrical activity in anatomically detailed ventricles. *Prog. Biophys. Mol. Biol.* 96, 19–43. doi: 10.1016/j.pbiomolbio.2007.07.004
- Dal, H., Göktepe, S., Kaliske, M., and Kuhl, E. (2013). A fully implicit finite element method for bidomain models of cardiac electromechanics. *Comput. Methods Appl. Mech. Eng.* 253, 323–336. doi: 10.1016/j.cma.2012.07.004
- D'Apolito, R., Tomaiuolo, G., Taraballi, F., Minardi, S., Kirui, D., Liu, X., et al. (2015). Red blood cells affect the margination of microparticles in synthetic microcapillaries and intravital microcirculation as a function of their size and shape. *J. Control Release.* 217, 263–272. doi: 10.1016/j.jconrel.2015.09.013
- Decker, K. F., Heijman, J., Silva, J. R., Hund, T. J., and Rudy, Y. (2009). Properties and ionic mechanisms of action potential adaptation, restitution, and accommodation in canine epicardium. *Am. J. Physiol. Heart Circ. Physiol.* 296, H1017–H1026. doi: 10.1152/ajpheart.01216.2008
- Ferrari, M. (2010). Frontiers in cancer nanomedicine: directing mass transport through biological barriers. *Trends Biotechnol.* 28, 181–188. doi: 10.1016/j.tibtech.2009.12.007
- Gerlowski, L. E., and Jain, R. K. (1986). Microvascular permeability of normal and neoplastic tissues. *Microvasc. Res.* 31, 288–305. doi: 10.1016/0026-2862(86)90018-X
- Hall, J. E. (2016). *Guyton and Hall Textbook of Medical Physiology, 13th Edn.* Philadelphia, PA: Elsevier.
- Henriquez, C. S. (1993). Simulating the electrical behavior of cardiac tissue using the bidomain model. *Crit. Rev. Biomed. Engng.* 21, 1–77.
- Henriquez, C. S., Muzikant, A. L., and Smoak, C. K. (1996). Anisotropy, fiber curvature, and bath loading effects on activation in thin and thick cardiac tissue preparations: simulations in a three-dimensional bidomain model. *J. Cardiovasc. Electrophysiol.* 7, 424–444. doi: 10.1111/j.1540-8167.1996.tb00548.x
- Hodkin, A. L., and Huxley, A. F. (1952). A quantitative description of membrane current and its application to conduction and excitation in nerve. *J. Physiol.* 117, 500–544. doi: 10.1113/jphysiol.1952.sp004764
- Hunter, P. J., McCulloch, A. D., and ter Keurs, H. E. (1998). Modelling the mechanical properties of cardiac muscle. *Prog. Biophys. Mol. Biol.* 69, 289–331. doi: 10.1016/S0079-6107(98)00013-3
- Ijiri, T., Ashihara, T., Yamaguchi, T., Takayama, K., Igarashi, T., and Shimada, T. (2008). A procedural method for modeling the Purkinje fibers of the heart. *J. Physiol. Sci.* 58, 481–486. doi: 10.2170/physiolsci.RP003208
- Isailovic, V., Kojic, M., Milosevic, M., Filipovic, N., Kojic, N., Ziemys, A., et al. (2014). A computational study of trajectories of micro- and nano-particles with different shapes in flow through small channels. *J. Serb. Soc. Comp. Mech.* 8, 14–28. doi: 10.5937/jsscm14020141
- Jain, R. (1987). Transport of molecules across tumor vasculature. *Cancer Metastasis Rev.* 6, 559–593. doi: 10.1007/BF00047468
- Jain, R. (1988). Determinants of tumor blood flow: a review. *Cancer Res.* 48, 2641–2658.
- Keener, J., and Sneyd, J. (2009). *Mathematical Physiology I: Cellular Physiology, II: Systems Physiology, 2nd Edn.* New York, NY: Springer.
- Keener, J. P., and Panfilov, A. V. (1996). A biophysical model for defibrillation of cardiac tissue. *Biophys. J.* 71, 1335–1345. doi: 10.1016/S0006-3495(96)79333-5
- Khaled, A.-R. A., and Vafai, K. (2003). The role of porous media in modeling flow and heat transfer in biological tissues. *Int. J. Heat Mass Transfer* 46, 4989–5003. doi: 10.1016/S0017-9310(03)00301-6
- Kim, N., Cannell, M. B., and Hunter, P. J. (2010). Changes in the calcium current among different transmural regions contributes to action potential heterogeneity in rat heart. *Prog. Biophys. Mol. Biol.* 103, 28–34. doi: 10.1016/j.pbiomolbio.2010.05.004
- Koay, E. J., and Ferrari, M. (2014). Transport oncophysics *in silico, in vitro, and in vivo.* *Preface Phys. Biol.* 11:060201. doi: 10.1088/1478-3975/11/6/060201
- Kojic, M. (2018). Smearred concept as a general methodology in finite element modeling of physical fields and mechanical problems in composite media. *J. Serbian Soc. Comput. Mech.* 12, 1–16. doi: 10.24874/jsscm.2018.12.02.01
- Kojic, M., and Bathe, K. J. (2005). *Inelastic Analysis of Solids and Structures.* Berlin, Heidelberg; New York, NY: Springer.
- Kojic, M., Filipovic, N., Stojanovic, B., and Kojic, N. (2008). *Computer Modeling in Bioengineering - Theoretical Background, Examples and Software.* Chichester: John Wiley and Sons.
- Kojic, M., Mijailovic, S., and Zdravkovic, N. (1998). Modelling of muscle behavior by the finite element method using Hill's three-element model. *Int. J. Num. Meth. Engng.* 43, 941–953. doi: 10.1002/(SICI)1097-0207(19981115)43:5<941::AID-NME435>3.0.CO;2-3
- Kojic, M., Milosevic, M., Simic, V., and Ferrari, M. (2014). A 1D pipe finite element with rigid and deformable walls. *J. Serb. Soc. Comp. Mech.* 8, 38–53. doi: 10.5937/jsscm1402038K
- Kojic, M., Milosevic, M., Simic, V., Geroski, V., Ziemys, A., Filipovic, N. (2019). Smearred multiscale finite element model for electrophysiology and ionic transport in biological tissue. *Comput. Biol. Med.* 108, 288–304. doi: 10.1016/j.combiomed.2019.03.023
- Kojic, M., Milosevic, M., Simic, V., Koay, E. J., Fleming, J. B., Nizzero, S., et al. (2017b). A composite smearred finite element for mass transport in capillary systems and biological tissue. *Comp. Meth. Appl. Mech. Engrg.* 324, 413–437. doi: 10.1016/j.cma.2017.06.019
- Kojic, M., Milosevic, M., Simic, V., Koay, E. J., Kojic, N., Ziemys, A., et al. (2017a). Extension of the Composite Smearred Finite Element (CSFE) to include lymphatic system in modeling mass transport in capillary systems and biological tissue. *J. Serb. Soc. Comp. Mech.* 11, 108–120. doi: 10.24874/jsscm.2017.11.02.09
- Kojic, M., Milosevic, M., Simic, V., Koay, E. J., Kojic, N., Ziemys, A., et al. (2018). Multiscale smearred finite element model for mass transport in biological tissue: from blood vessels to cells and cellular organelles. *Comput. Biol. Med.* 99, 7–23. doi: 10.1016/j.combiomed.2018.05.022
- Kojic, M., Slavkovic, R., Zivkovic, M., Grujovic, N., Filipovic, N., and Milosevic, M. (2010). *PAK - Finite Element Program for Linear and Nonlinear Analysis.* Kragujevac: Univ Kragujevac and R&D Center for Bioengineering.
- Kojić, N., Milošević, M., Petrović, D., Isailović, V., Sarioglu, A. F., Haber, D. A., et al. (2015). A computational study of circulating large tumor cells traversing microvessels. *Comput. Biol. Med.* 63, 187–195. doi: 10.1016/j.combiomed.2015.05.024
- Lafortune, P., Aris, R., Vázquez, M., and Houzeaux, G. (2012). Coupled electromechanical model of the heart: parallel finite element formulation. *Int. J. Numer. Meth. Biomed. Engng.* 28, 72–86. doi: 10.1002/cnm.1494
- Lauffenburger, D. A., and Horwitz, A. F. (1996). Cell migration: review a physically integrated molecular process. *Cell* 84, 359–369. doi: 10.1016/S0092-8674(00)81280-5
- Less, J. R., Skalak, T. C., Sevcik, E. M., and Jain, R. K. (1991). Microvascular architecture in a mammary carcinoma: branching patterns and vessel dimensions. *Cancer Res.* 51, 265–273.
- Ma, P. X., and Zhang, R. (1998). Synthetic nano-scale fibrous extracellular matrix. *J. Biomed. Mater. Res.* 46, 60–72. doi: 10.1002/(SICI)1097-4636(199907)46:1<60::AID-JBM7>3.0.CO;2-H

- Mathura, K. R., Vollebregt, K. C., Boer, K., De Graaff, J. C., Ubbink, D. T., and Ince, C. (2001). Comparison of OPS imaging and conventional capillary microscopy to study the human microcirculation. *J. Appl. Physiol.* 91, 74–78. doi: 10.1152/jappl.2001.91.1.74
- Mijailovich, S. M., Stojanovic, B., Kojic, M., Liang, A., Wedeen, V. J., and Gilbert, R. J. (2010). Derivation of a finite-element model of lingual deformation during swallowing from the mechanics of mesoscale myofiber tracts obtained by MRI. *J. Appl. Physiol.* 109, 1500–1514. doi: 10.1152/japplphysiol.00493.2010
- Milosevic, M., Simic, V., Milicevic, B., Koay, E. J., Ferrari, M., Ziemys, A., et al. (2018a). Correction function for accuracy improvement of the composite smearred finite element for diffusive transport in biological tissue systems. *Comp. Meth. Appl. Mech. Engrg.* 338, 97–116. doi: 10.1016/j.cma.2018.04.012
- Milosevic, M., Stojanovic, D., Simic, V., Milicevic, B., Radisavljevic, A., Uskokovic, P., et al. (2018b). A computational model for drug release from PLGA implant. *Materials* 11:2416. doi: 10.3390/ma1122416
- Moraru, I. I., Schaff, J. C., Slepchenko, B. M., Blinov, M. L., Morgan, F., Lakshminarayana, A., et al. (2008). Virtual Cell modelling and simulation software environment. *IET Syst. Biol.* 2, 352–362. doi: 10.1049/iet-syb:20080102
- Nicholson, C. (2001). Diffusion and related transport mechanisms in brain tissue. *Rep. Prog. Phys.* 64, 815–884. doi: 10.1088/0034-4885/64/7/202
- Noble, D. (1962). A modification of the Hodgkin-Huxley equations applicable to Purkinje fibre action and pace-maker potentials. *J. Physiology.* 160, 317–352. doi: 10.1113/jphysiol.1962.sp006849
- Nugent, L. J., and Jain, R. K. (1984). Extravascular diffusion in normal and neoplastic tissues. *Cancer Res.* 44, 238–244.
- O'Hara, T., Virág, L., Varró, A., and Rudy, Y. (2011). Simulation of the undiseased human cardiac ventricular action potential: Model formulation and experimental validation. *PLoS Comput. Biol.* 7:e1002061–e1002090. doi: 10.1371/journal.pcbi.1002061
- Popel, A. S., and Pittman, R. N. (1998). “The microcirculation physiome,” in *Handbook of Biomedical Engineering*, ed J. Bronzino (Boca Raton, FL: CRC Press), 911–913.
- Rangamani, P., and Iyengar, R. (2007). Modelling spatio-temporal interactions within the cell. *J. Biosci.* 32, 157–167. doi: 10.1007/s12038-007-0014-3
- Reulen, H. J., Graham, R., Spatz, M., and Klatzo, I. (1977). Role of pressure gradients and bulk flow in dynamics of vasogenic brain edema. *J. Neurosurg.* 46, 24–35. doi: 10.3171/jns.1977.46.1.0024
- Roberts, W. G., and Palade, G. E. (1997). Neovasculature induced by vascular endothelial growth factor is fenestrated. *Cancer Res.* 57, 765–772.
- Rocha, B. M., Kicking, F., Prassl, A. J., Haase, G., Vigmond, E. J., dos Santos, R.W., et al. (2011). A macro finite element formulation for cardiac electrophysiology simulations using hybrid unstructured grids. *IEEE Trans Biomed Eng.* 58, 1055–1065. doi: 10.1109/TBME.2010.2064167
- Roth, B. J., and Wikswo, J. P. (1986). A bidomain model for the extracellular potential and magnetic field of cardiac tissue. *IEEE Trans. Biomed. Engrg.* 33, 467–469. doi: 10.1109/TBME.1986.325804
- Rushmer, R. F. (1976). *Cardiovascular Dynamics, 4th Edn.* Philadelphia, PA: W. B. Saunders Co.
- Santiago, A. (2018). *Fluid-Electro-Mechanical Model of the Human Heart for Supercomputers*. Barcelona: Universitat Politècnica de Catalunya.
- Schaff, J., Fink, C. C., Slepchenko, B., Carson, J. H., and Loew, L. M. (1997). A general computational framework for modeling cellular structure and function. *Biophys. J.* 73, 1135–1146. doi: 10.1016/S0006-3495(97)78146-3
- Sevick, E. M., and Jain, R. K. (1989a). Geometric resistance to blood flow in solid tumors perfused *ex vivo*: Effects of tumor size and perfusion pressure. *Cancer Res.* 49, 3506–3512.
- Sevick, E. M., and Jain, R. K. (1989b). Viscous resistance to blood flow in solid tumors: effect of hematocrit on intratumor blood viscosity. *Cancer Res.* 49, 3513–3519.
- Sevick, E. M., and Jain, R. K. (1991). Effect of red blood cell rigidity on tumor blood flow: increase in viscous resistance during hyperglycemia. *Cancer Res.* 51, 2727–2730.
- Shi, Y., Lawford, P., and Hose, R. (2011). Review of zero-D and 1-D models of blood flow in the cardiovascular system. *Biomed. Eng.* 10:33. doi: 10.1186/1475-925X-10-33
- Skinner, S. A., Tutton, P. J., and O'Brien, P. E. (1990). Microvascular architecture of experimental colon tumors in the rat. *Cancer Res.* 50, 2411–2417.
- Slepchenko, B. M., Schaff, J. C., Macara, I., and Loew, L. M. (2003). Quantitative cell biology with the Virtual Cell. *Trends Cell Biol.* 13, 570–576. doi: 10.1016/j.tcb.2003.09.002
- Smith, N. P., Pullan, A. J., and Hunter, P. J. (2002). An anatomically based model of transient coronary blood flow in the heart. *SIAM J. Appl. Math.* 62, 990–1018. doi: 10.1137/S0036139999355199
- Stojanovic, B., Kojic, M., Rosic, M., Tsui, C. P., and Tang, C. Y. (2007). An extension of Hill's three-component model to include different fiber types in finite element modelling of muscle. *Int. J. Num. Meth. Eng.* 71, 801–817. doi: 10.1002/nme.1963
- Sun, H., and Pang, K. S. (2008). Transport, and metabolism of solutes in Caco-2 cell monolayers: a theoretical study. *Drug Metabol. Dispos.* 36, 102–123. doi: 10.1124/dmd.107.015321
- Swabb, E. A., Wei, J., and Gullino, P. M. (1974). Diffusion and convection in normal and neoplastic tissues. *Cancer Res.* 34, 2814–2822.
- Trapp, S., and Horobin, R. W. (2005). A predictive model for the selective accumulation of chemicals in tumor cells. *Eur. Biophys. J.* 34, 959–966. doi: 10.1007/s00249-005-0472-1
- Vigmond, E. J., and Stuyvers, B. D. (2016). Modeling our understanding of the His-Purkinje system. *Prog. Biophys. Mol. Biol.* 120, 179–188. doi: 10.1016/j.pbiomolbio.2015.12.013
- Winslow, R. L. (1992). *Theoretical Foundations of Neural Modeling*. BME 580.681. Baltimore: The John Hopkins Univ. Sch. Medicine and Whiting Sch Engrg.
- Zagorchev, L., Oses, P., Zhuang, Z. W., Moodie, K., Mulligan-Kehoe, M. J., Simons, M., et al. (2010). Micro computed tomography for vascular exploration. *J Angiogenesis Res.* 2:7. doi: 10.1186/2040-2384-2-7

Conflict of Interest: The authors declare that the research was conducted in the absence of any commercial or financial relationships that could be construed as a potential conflict of interest.

Copyright © 2019 Kojic, Milosevic, Simic, Milicevic, Geroski, Nizzero, Ziemys, Filipovic and Ferrari. This is an open-access article distributed under the terms of the Creative Commons Attribution License (CC BY). The use, distribution or reproduction in other forums is permitted, provided the original author(s) and the copyright owner(s) are credited and that the original publication in this journal is cited, in accordance with accepted academic practice. No use, distribution or reproduction is permitted which does not comply with these terms.